

## Scalar Aharonov-Bohm effect with longitudinally polarized neutrons

B. E. Allman,<sup>1</sup> W.-T. Lee,<sup>2</sup> O. I. Motrunich,<sup>3</sup> and S. A. Werner<sup>4</sup>

<sup>1</sup>*School of Physics, University of Melbourne, Parkville, Australia 3052*

<sup>2</sup>*Oak Ridge National Laboratory, Oak Ridge, Tennessee 37831*

<sup>3</sup>*Physics Department, Princeton University, Princeton, New Jersey 08544*

<sup>4</sup>*Department of Physics and Astronomy and Research Reactor Center, University of Missouri–Columbia, Columbia, Missouri 65211*

(Received 19 April 1999)

In the scalar Aharonov-Bohm effect, a charged particle (electron) interacts with the scalar electrostatic potential  $U$  in the field-free (i.e., force-free) region inside an electrostatic cylinder (Faraday cage). Using a perfect single-crystal neutron interferometer we have performed a “dual” scalar Aharonov-Bohm experiment by subjecting polarized thermal neutrons to a pulsed magnetic field. The pulsed magnetic field was spatially uniform, precluding any force on the neutrons. Aligning the direction of the pulsed magnetic field to the neutron magnetic moment also rules out any classical torque acting to change the neutron polarization. The observed phase shift is purely quantum mechanical in origin. A detailed description of the experiment, performed at the University of Missouri Research Reactor, and its interpretation is given in this paper. [S1050-2947(99)02310-0]

PACS number(s): 03.65.Bz, 03.75.Dg, 42.50.-p

### I. AHARONOV-BOHM EFFECTS

In classical mechanics, the presence of a potential can only be inferred from the motion of a particle under the influence of the force a spatially nonuniform potential generates. The motion (kinematics) of a particle through a region of uniform potential is no different from that through empty space. However, in quantum mechanics the primary physical significance of the potential becomes apparent. The de Broglie wave of a particle passing through a potential, uniform or not, acquires a phase shift due to its interaction with the potential. In 1959, Aharonov and Bohm (AB) proposed two electron interference experiments [1] to observe such an effect, a work that has since spawned many hundreds of papers [2]. In the AB experiments, the wave function of the electron obeys the time-dependent Schrödinger equation

$$(H_0 + V)\Psi = \frac{i\hbar \partial \Psi}{\partial t}, \quad (1)$$

where  $V = -eU$  and  $H_0 = \mathbf{p}^2/2m$ , with  $\mathbf{p}$  the canonical momentum given by

$$\mathbf{p} = m\mathbf{v} + \frac{e}{c}\mathbf{A}. \quad (2)$$

In these equations,  $U$  is the scalar electrostatic potential,  $m\mathbf{v}$  is the classical momentum of the electron, and  $\mathbf{A}$  is the vector electromagnetic potential. These effects manifest themselves as a shift of the phase of the quantum-mechanical wave function, while the energy remains unchanged. An interference experiment offers the opportunity to measure this phase shift.

#### A. Aharonov-Bohm experiments

The effects Aharonov and Bohm proposed are of two versions, scalar (or electric) and vector (or magnetic) AB ef-

fects, and are shown in Fig. 1. They appear as the scalar and vector terms of the four vector in the temporal and spatial parts, respectively, of the action integral describing the interaction. Historically, they have been studied in reverse order. In the vector AB experiment [Fig. 1(a)], the electron experiences a vector potential as it diffracts in the field-free (i.e., force-free) region on either side of a magnetic flux tube. The phase shift of the electron wave function is given by the spatial path integral of the canonical momentum

$$\Delta\phi_{AB} = \frac{1}{\hbar} \oint \mathbf{p} \cdot d\mathbf{s} = \frac{e}{\hbar c} \oint \mathbf{A}(\mathbf{x}') \cdot d\mathbf{x}' = \frac{e}{\hbar c} \Phi_M, \quad (3)$$

where  $\Phi_M$  is the total magnetic flux enclosed by the two paths. This effect had been observed in a series of investigations culminating in the unequivocal experiment of Tonomura *et al.* [3], using a modified electron microscope and a copper- and niobium-coated superconducting permalloy toroid as the line of flux.

For the scalar AB experiment [Fig. 1(b)], the electron passes along the axis of an electrostatic cylinder (Faraday cage) to which a time-dependent electrostatic potential is applied while the electron is entirely enclosed within, a condition guaranteeing the interaction is in the absence of an electromagnetic field. The phase shift is now given by the temporal part of the action integral

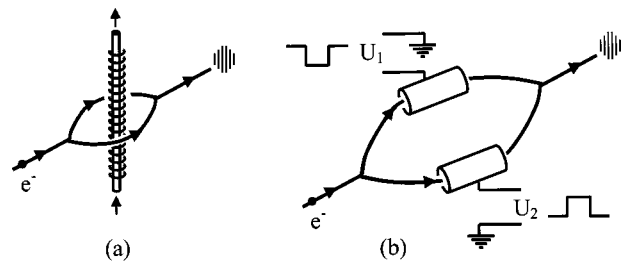


FIG. 1. Schematic of the (a) vector and (b) scalar Aharonov-Bohm electron interferometry experiments.

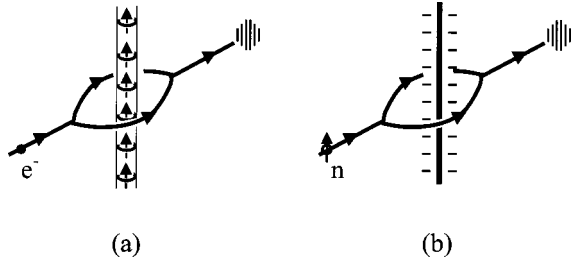


FIG. 2. (a) Schematic of the vector AB experiment, where the tube of magnetic flux has been replaced by a line of magnetic dipoles. (b) The Aharonov-Casher dual experiment where the magnetic dipole (neutron) diffracts around a line of electric charge.

$$\begin{aligned}\Delta\phi_{AB} &= -\frac{1}{\hbar} \oint \Delta H(t') dt' \\ &= -\frac{e}{\hbar} \oint_{\delta t \text{ pulse}} U(t') dt' = -\frac{e}{\hbar} U_{AV} \delta t.\end{aligned}\quad (4)$$

The scalar AB effect described here has yet to be observed due to extreme difficulties in setting up the experiment. The forces acting on the electrons render the experiment by Ma-teucci and Pozzi [4] inconclusive.

### B. Neutron analog Aharonov-Bohm experiments

According to the standard minimal-coupling scheme, a particle like a neutron should not experience a vector AB effect due to its electrical neutrality. This was shown to be the case experimentally, using a perfect crystal neutron interferometer in a topology similar to Fig. 1(a) [5].

In 1984 Aharonov and Casher (AC) suggested the electromagnetic and quantum mechanical dual of the vector AB effect [6], a suggestion that had independently been made earlier by Hraskó [7] and Farago [8]. If the line of magnetic flux [Fig. 1(a)] is replaced with a line of magnetic dipoles [Fig. 2(a)], then, in the reference frame of the electron, we have the theoretical and topological equivalent [9,10] of a magnetic dipole (e.g., a neutron) diffracting around a line of electric charge [Fig. 2(b)]. Such an experiment was performed by Cimmino *et al.* [11] in 1989, using a neutron diffracting around a prism electrode assembly. The charged electrode was identical to a continuous series of line charges residing on its surfaces. The canonical momentum of a neutron having magnetic moment  $\boldsymbol{\mu}$ , mass  $m$ , and velocity  $\mathbf{v}$ , in an electric field  $\mathbf{E}$ , is

$$\mathbf{p} = m\mathbf{v} + \frac{\boldsymbol{\mu}}{c} \times \mathbf{E}. \quad (5)$$

The phase shift due to the  $\boldsymbol{\mu} \times \mathbf{E}$  term for a neutron moving through a constant electric field has been calculated [12]. Although the experimental geometry of Cimmino *et al.* contains three vector components—the neutron magnetic moment, the electric field, and the direction of motion of the neutron—they can be arranged to be mutually orthogonal so that the effective magnetic field,  $\mathbf{B}' = -(\mathbf{v}/c) \times \mathbf{E}$ , that the moving neutron “feels” in its rest frame, is parallel to  $\boldsymbol{\mu}$ . In this case, no classical force on the neutron is generated [13]. Under such conditions

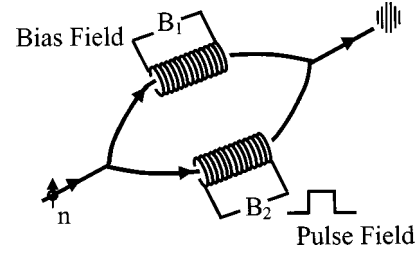


FIG. 3. Schematic of the dual scalar AB experiment for neutrons. The wave form for the applied current pulses is also shown.

$$\boldsymbol{\mu} \times \mathbf{E} = \frac{2\sigma\mu\Lambda}{r} \hat{\boldsymbol{\phi}}, \quad (6)$$

is seen to be a solenoidal vector field (like  $\vec{A}$  outside of a solenoid), where  $\hat{\boldsymbol{\phi}}$  is the azimuthal unit vector, and the phase shift becomes

$$\Delta\phi_{AC} = \frac{1}{\hbar} \oint \mathbf{p} \cdot d\mathbf{s} = \frac{1}{\hbar c} \oint \boldsymbol{\mu} \times \mathbf{E} \cdot d\mathbf{s} = \sigma \frac{4\pi\mu\Lambda}{\hbar c}. \quad (7)$$

$\Lambda$  is the enclosed linear charge density, and  $\sigma = \pm 1$  depends on whether the neutron spin is parallel or antiparallel to the axis of the line charge. This phase shift is seen even though the velocity of the neutron is unchanged.

Similarly, a dual neutron experiment was first suggested by Zeilinger [14], and later by Anandan [15], for the scalar AB effect. The experiment was subsequently performed by Allman *et al.* using unpolarized incident neutrons [16]. In this experiment, shown in Fig. 3, a time-dependent current pulse is applied to a solenoid in one arm of the neutron interferometer, while the neutron wave packet is completely contained within its uniform magnetic-field region. The scalar interaction (dual of the scalar electrostatic potential) in this geometry is

$$V(t) = -\boldsymbol{\mu} \cdot \mathbf{B}(t), \quad (8)$$

where  $\mathbf{B}(t)$  is the pulsed magnetic field. It produces a quantum-mechanical phase shift, measurable by neutron interferometry, though the neutron experiences no field gradient and hence no force. The phase shift is given by

$$\Delta\phi_{AB} = -\frac{1}{\hbar} \oint \Delta H(t') dt' = -\frac{\sigma\mu}{\hbar} \oint_{\delta t \text{ pulse}} B(t') dt', \quad (9)$$

the analog of Eq. (4). A further polarimetry experiment [17] showed the nondispersive nature and momentum conservation of this experimental setup by comparing a pulsed magnetic-field measurement with that for a static field. For the static field  $\mathbf{B} = \mathbf{B}(\mathbf{x})$ , a field gradient and hence a conservative force exist, given by

$$\mathbf{F} = \nabla \boldsymbol{\mu} \cdot \mathbf{B}(\mathbf{x}), \quad (10)$$

and the phase shift becomes

$$\Delta\phi_{AB} = \frac{1}{\hbar} \oint \Delta \mathbf{p} \cdot d\mathbf{x} = \frac{1}{\hbar} \oint m \Delta \mathbf{v} \cdot d\mathbf{x} = \frac{\sigma\mu}{\hbar} \oint_{\delta t} \mathbf{B}(\mathbf{x}) \cdot d\mathbf{x}. \quad (11)$$

This phase shift is a consequence of a change in velocity (momentum) of the neutron given by

$$\Delta v = \frac{\mu B}{m v_0}, \quad (12)$$

though the energy remains constant. This experiment exhibits Zeeman splitting in a longitudinal Stern-Gerlach experiment. The impact of the dispersive interaction is to spatially spread and separate the interfering wave packets, and thus reduce the interference contrast. It remains an experimental challenge to make the relative displacement of the two wave packets a significant fraction of the coherence length, and observe this loss of contrast in a neutron interferometry experiment.

The reader might assume that the use of polarized neutrons is essential for both the neutron scalar AB and AC experiments. This requirement has led to some interpretational objections [18,19]. In both experiments a quantization axis for the neutron spin was defined by an appropriately oriented environmental magnetic field that encompassed the interferometer (normal to the plane of the interferometer in the AC case, and longitudinally for the scalar AB). The unpolarized neutron could then be considered as the appropriate incoherent mixture of parallel and antiparallel components [20]. In the case of the scalar AB experiment, it was argued [18] that even though the neutron experienced no classical force, a vertically polarized neutron, say, would experience a classical torque  $\boldsymbol{\tau} = \boldsymbol{\mu} \times \mathbf{B}$  and therefore precess about the longitudinal pulsed magnetic field with Larmor frequency  $\omega_L = 2\mu B/\hbar$ . Such precession would change the spin orientation by an angle  $\phi_L = \omega_L \delta t$ , an effect that could be measured by polarimetry. Here, the phase shift is found again using Eq. (9), but is the result of a Larmor precession

$$\begin{aligned} \Delta \phi_{AB} &= -\frac{1}{\hbar} \oint \Delta H(t') dt' \\ &= -\frac{\sigma \mu}{\hbar} \oint_{\delta t \text{ pulse}} B(t') dt' = -\frac{\sigma \phi_L}{2}, \end{aligned} \quad (13)$$

that could be measured by polarization analysis [17]. We have now carried out a scalar AB (SAB) experiment similar to the original using neutrons polarized along the pulsed  $\mathbf{B}(t)$  field to remove such a possible measurement and interpretation. A brief account of the results of this experiment has already been reported [21]. In this arrangement, there is neither a classical torque nor (as before) a classical force exerted on the neutron, and the results achieved are essentially the same as for an unpolarized neutron experiment.

### C. Atom Aharonov-Bohm experiments

In principle, the AB effects are much greater for atoms than for neutrons, by a factor of the order of the ratio (Bohr magneton)/(nuclear magneton), i.e.,  $\approx m_n/m_e$ , and thus much higher precision should be attainable. Recently a number of atomic AB experiments analogous to the neutron experiments have been performed. An atom interferometric scalar AB experiment [22] was performed using a beam of metastable hydrogen atoms, and represents the quantum-mechanical and topological equivalent of the neutron experi-

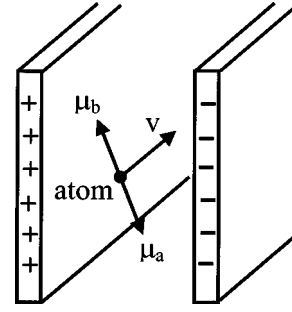


FIG. 4. Schematic of the atomic AC experiment. The atoms travel the same path through a uniform electric field as a coherent superposition of opposite magnetic moments.

ment of Ref. [17], that is, a polarimetry measurement. A series of atomic AC experiments [23,24,25] have also been performed, and have measured the phase shift to an accuracy of a few percent. However, the experimental geometry of these experiments does not represent the topological equivalent of the neutron AC experiment, or, for that matter, the original vector AB effect [26]. The geometry of the atomic AC experiments is shown in Fig. 4, wherein oppositely polarized atomic subbeams pass between a pair of electrodes. That is, the interferometer arms are distinguished not by separated trajectories, but by internal degrees of freedom, magnetic quantum numbers. We note that interference in spin space may be interpreted classically as the alignment of the spins, and may be measured by polarimetry. This is not possible for the interference of beams following two different paths in space, as in the neutron AC geometry, as there is no classical analogy to the probability amplitude of two-path superposition [27]. The robustness of the topological nature of the AC effect is embedded in the interference paths completely encircling the line charge, i.e., a winding number 1, and is independent of where the line charge singularity occurs within the interference loop. The atomic AC experiments only show the velocity independence and the proportionality to the electric field of the AC phase shift.

## II. EXPERIMENTAL SETUP

The experiment shown schematically in Fig. 5 was performed with the neutron interferometry apparatus at beam port C of the University of Missouri Research Reactor [28]. A collimated, nominally monochromatic beam of 2.35 Å neutrons ( $\delta\lambda/\lambda \approx 0.012$ ) from a vertically focusing 0.4° mosaic Pyrolytic Graphite (002) crystal is directed onto the interferometer setup. The apparatus consists of two main parts—the neutron polarizer and the neutron interferometer—and works on the polarization dependence (birefringence) of the neutron index of refraction in a magnetic field and the arc second angular resolution of the Bragg reflection from a perfect crystal. A photograph of the setup is shown in Fig. 6, the components of which will now be discussed in turn.

### A. Neutron polarizer—double-bounce crystal

The neutron polarizer includes a two-blade, double-bounce neutron reflector cut from a perfect single silicon crystal and a magnetic prism assembly. This polarizer is dif-

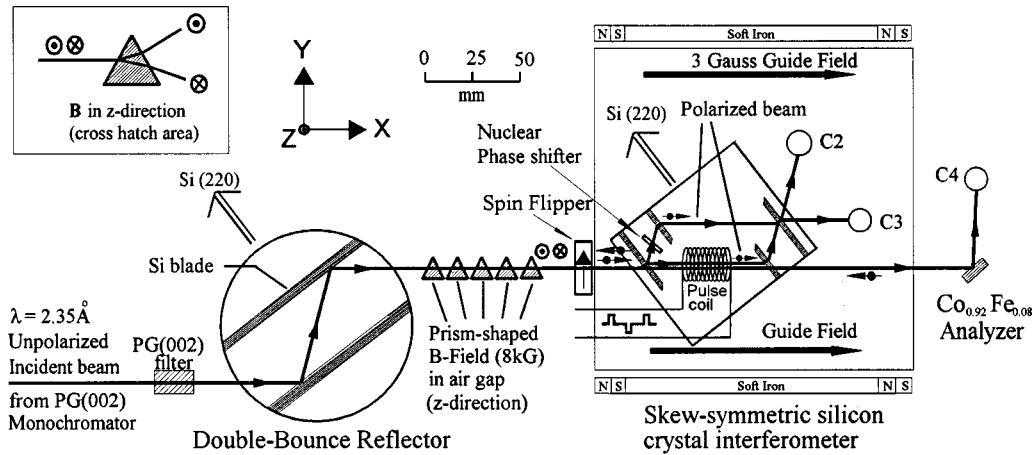


FIG. 5. Schematic of the experimental setup. The polarizer consists of the perfect single silicon crystal double bounce reflector and the series of five prism-shaped air-gap magnetic fields. The silicon skew-symmetric interferometer crystal and the “Pulse” coil are the key components with which to observe the SAB effect. A static-type spin flipper is placed between the polarizer and the interferometer to rotate the neutron spins from the  $z$  direction to the longitudinal  $x$  direction. The permanent magnet guide field maintains this direction of polarization throughout the region of the interferometer. Behind the interferometer is a magnetically saturated  $\text{Co}_{0.92}\text{Fe}_{0.08}(111)$  crystal to analyze the classical spin orientation. The inset shows the birefringent splitting of the two polarization states.

ferent from the conventional methods which employ reflections from magnetized crystals like  $\text{Fe}_3\text{O}_4$ ,  $\text{Co}_{0.98}\text{Fe}_{0.08}$ , the Heusler alloy  $\text{Cu}_2\text{MnAl}$ , or magnetic supermirrors [29,30]. Our method is similar to the neutron optical technique historically employed by the Vienna neutron interferometry group at Institut Laue Langevin [31]. The double-bounce method has the advantage that the outgoing beam is parallel to the incident beam and the simple removal of the magnetic prism assembly allows for the use of unpolarized neutrons with minimal realignment of the setup downstream. The double-bounce crystal is machined so that the (220) reciprocal-lattice vector is perpendicular to the crystal blade surface. A photograph of the crystal mounted on fine and coarse rotation stages and a tilt stage is shown in Fig. 7. Only those neutrons that fall within the Darwin width  $\Delta\theta_D = 1.6$  arc sec of the Bragg condition ( $\lambda = 2d \sin \theta_B$ ) are reflected by both blades of the reflector. The Darwin width  $\Delta\theta_D$  derived from dynamical diffraction theory is given by

$$\Delta\theta_D = \frac{2\lambda^2 F_{220}}{\pi V_x \sin 2\theta_B}, \quad (14)$$

where  $F_{220}$  is the structure factor for the (220) reflection and  $V_x$  is the volume of the silicon unit cell. The dynamical



FIG. 6. A photograph of the experimental setup at beam port C at the University of Missouri Research Reactor. The neutron beam enters from the left and the double bounce crystal, prism assembly, interferometer crystal, analyzer, and neutron detectors are clearly seen.

diffraction theory mean reflectivity of a single Bragg reflection in a thick crystal is given by

$$\bar{R}^B = \begin{cases} 1, & |x| < 1 \\ 1 - \left(1 - \frac{1}{x^2}\right)^{1/2}, & |x| \geq 1, \end{cases} \quad (15)$$

with

$$x = \frac{\Delta\theta}{\Delta\theta_D}, \quad (16)$$

where  $\Delta\theta$  is the rocking angle. This mean reflectivity profile is shown in Fig. 8(a). The integrated reflected intensity is found by

$$\mathcal{I} = \int_{-\infty}^{\infty} \bar{R} dx. \quad (17)$$

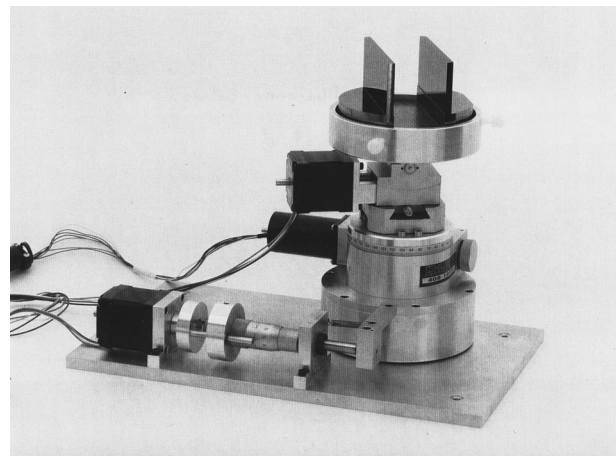


FIG. 7. A photograph of the double-bounce perfect silicon crystal mounted on its tilt, coarse rotation, and fine rotation stages (top to bottom).

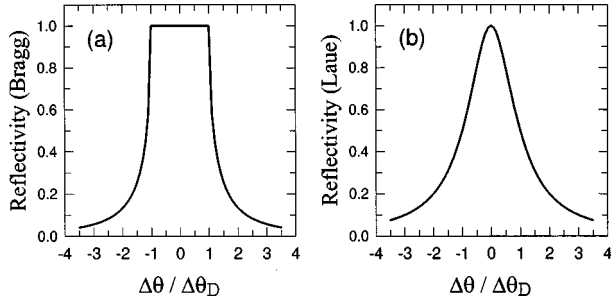


FIG. 8. Reflectivity profile for (a) Bragg and (b) Laue reflection from a thick perfect single crystal.

For a single Bragg (SB) reflection this is

$$\mathcal{I}^{\text{SB}} = \int_{-\infty}^{\infty} \bar{R}^{\text{SB}} dx = \pi \theta_D, \quad (18)$$

and, for a double reflection,

$$\mathcal{I}^{\text{DB}} = \int_{-\infty}^{\infty} (\bar{R}^{\text{SB}})^2 dx = (2\pi - 4)\theta_D. \quad (19)$$

The relative intensity of the double bounce to the single bounce is therefore

$$\frac{\mathcal{I}^{\text{DB}}}{\mathcal{I}^{\text{SB}}} = \frac{(2\pi - 4)\theta_D}{\pi\theta_D} = 0.727; \quad (20)$$

that is, 73% of the neutrons reflected by the first blade will be reflected by the second. Figure 9 shows a plot of the experimental single and double reflection intensity profiles which agree with the theoretical prediction.

### B. Neutron polarizer–magnetic prism assembly

The neutrons selected by the double-bounce crystal then travel through the air gap between five pairs of prism-shaped  $\text{Nd}_2\text{Fe}_{14}\text{B}$  magnets of the prism assembly. Each magnet pair produces a vertical magnetic field  $\mathbf{B} = B(x, y)\hat{\mathbf{z}}$  of about 8 kG

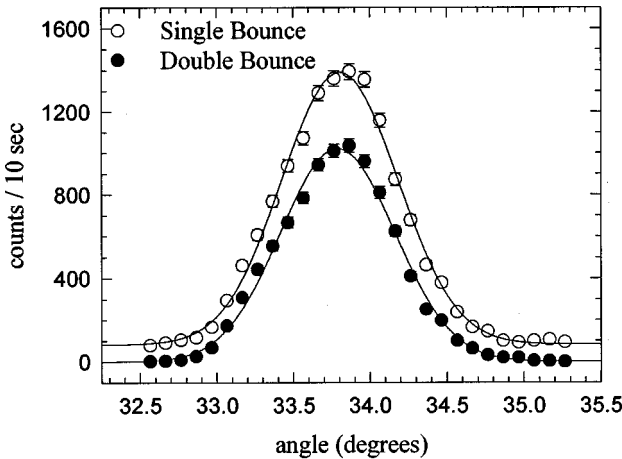


FIG. 9. Rocking curves for the single and double Bragg reflections of the double-bounce reflector. The intensity ratio of the double reflection to the single reflection is about 72%, the same as the predicted value from dynamical diffraction theory.

in the 5-mm air gap between them. The interaction potential between the neutron magnetic moment and the magnetic field leads to two indices of refraction (birefringence) for the neutron spin states  $\sigma = \pm 1$  for the neutron spins parallel and antiparallel to the field given by

$$n_{\pm} = 1 \mp \frac{\mu B}{m v^2} = 1 \mp \varepsilon. \quad (21)$$

Coupled with the boundary condition of the neutron wave function entering and leaving the region of magnetic field, the prism field acts to refract the two spin states into slightly diverging directions (inset of Fig. 5). The angle of deviation from the incident direction is

$$\delta_{\pm} = \mp \varepsilon \tan \frac{\alpha}{2}, \quad (22)$$

where  $\alpha = 60^\circ$  is the prism apex angle. The return field of the prism-shaped magnets is carried by a soft-iron yoke in contact with the back surfaces of the magnets. The yoke reduces fringing fields at either end of the prism assembly, an imperative when trying to control the neutron polarization accurately.

### C. Spin flipper

A static spin flipper with  $\mathbf{B} \approx B_{\text{SF}}\hat{\mathbf{y}}$  is placed in the beam path between the prism field assembly and the interferometer to rotate the neutron polarization from the vertical  $\mathbf{z}$  direction to the longitudinal  $\mathbf{x}$  direction. The flipper coil consists of 13 layers of anodized aluminum foil formed on a rectangular aluminum frame that is 12.5 mm along the beam path and 12.5 mm high by 50 mm wide. To compensate for stray magnetic fields in the  $y$ - $z$  plane, the spin flipper is mounted on a tilt stage that rotates about the longitudinal  $x$  axis. The rotation of the neutron spin about the  $z$  axis to the longitudinal direction is optimized by the flipper field strength. Finally, the spin flipper is enclosed in a steel box, with openings for the beam to pass through, to improve the isolation of the spin flipper field from both the vertical fringe field of the prism assembly and the longitudinal guide field enveloping the interferometer. An additional high magnetic permeability mumetal enclosure placed between the prism assembly and spin flipper further reduced fringe fields from the longitudinal guide field.

### D. Guide field

An experimentally optimized, uniform 3-G longitudinal guide field to maintain the neutron's polarization is established throughout the aluminum interferometer housing. The guide field is produced by four horizontal bar magnets that span the entire length of the aluminum box placed at the top and bottom edge of each side of the box running parallel to the beam direction. Each bar magnet is made by embedding two small  $\text{Nd}_2\text{Fe}_{14}\text{B}$  magnets between three, long soft iron bars, and placing a larger, weaker Alnico magnet at each end. This configuration forces the return field of the magnetic octupole to run longitudinally along the beam path.

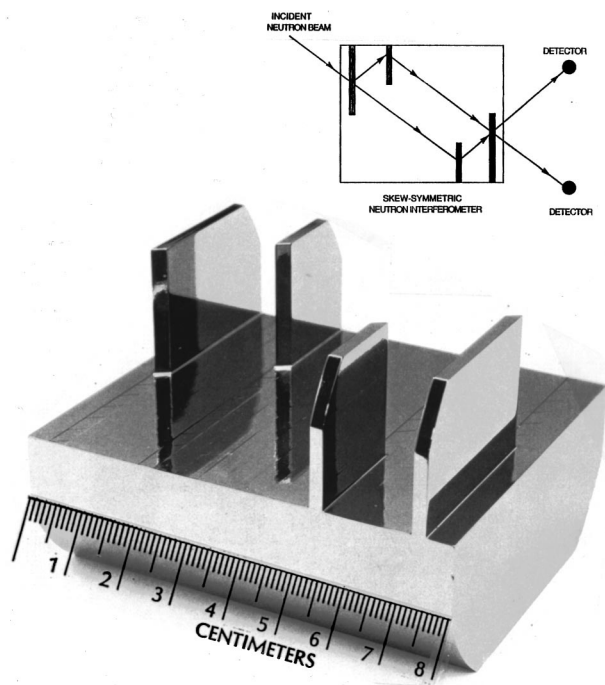


FIG. 10. A photograph of the skew-symmetric Laue-Lau-Lau perfect single-silicon-crystal neutron interferometer.

Further experimentally prescribed steel plates and mumetal sheets are mounted at the front and rear of the aluminum box, to control fringe fields.

#### E. Neutron interferometer

The monolithic, four-blade skew-symmetric, perfect single-silicon-crystal neutron interferometer further downstream also uses the Si(220) reflection, but in Laue geometry. A photograph of the interferometer is shown in Fig. 10. The incident neutrons are Bragg diffracted by the first crystal plate dividing the incident de Broglie wave front into two coherent subbeams. Each of these is deflected by diffraction at the intermediate crystal plates and after traversing a solenoid on path I (marked “pulse coil” in Fig. 5), the two beams recombine at the last crystal plate. The whole arrangement is akin to the Mach-Zehnder interferometer of classical optics.

The neutron interferometer also has an angular acceptance equal to the Darwin width. The Laue mean reflectivity profile for a thick crystal is given by

$$\bar{R}^L = \frac{1}{2(1+x^2)}, \quad (23)$$

where  $x$  is defined in Eq. (16), and the profile shown in Fig. 8(b). The integrated intensities in the detected C2 and C3 detector beams of the interferometer are then a result of the two Bragg reflections in the double bounce reflector and the appropriate combination of Laue reflections and transmissions in the interferometer.

#### F. Pulse coil

Central to the force-free nature of the experiment is the spatially uniform pulsed magnetic field inside the interferom-

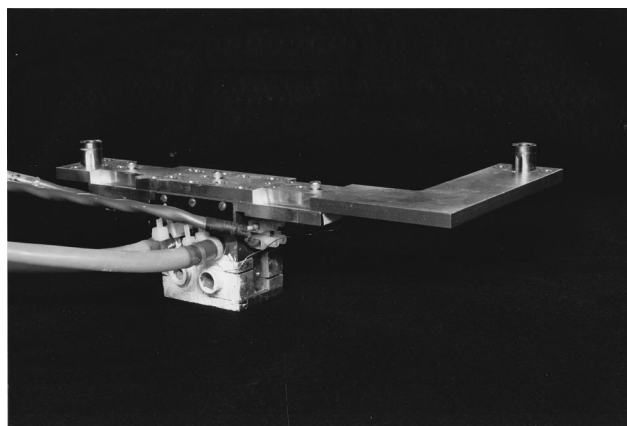


FIG. 11. Photograph of the coil assembly, showing the “bias” (near) and “pulse” (far) solenoids mounted in their aluminum blocks and water-cooled copper frame. The face of the assembly has been painted with white, neutron-absorbing  $\text{Gd}_2\text{O}_3$  paint.

eter. This field was provided by the “pulse” coil, a 45-mm-long solenoid of  $\sim 160$  turns wound in a tightly packed single layer onto a 7-mm inner diameter insulating (to reduce eddy currents) phenolic former. Placing trim coils at each end of the single layer yielded a 28-mm-long region of field uniform to 1%, equivalent to a  $16\text{-}\mu\text{sec}$  neutron flight transit time. This is twice the  $8\text{-}\mu\text{sec}$  current pulse ( $< 1\text{-}\mu\text{sec}$  rise time) applied to the “pulse” coil. The solenoid is sealed at the end with aluminum foil and has a slotted (again to reduce eddy currents) aluminum casing. This combination is snugly mounted in aluminum blocks in a water-cooled copper locating frame all in good thermal contact to conduct Joule heating away from the solenoid, and hence from the interferometer. The regulation of the temperature inside the interferometer was maintained to  $0.2^\circ\text{C}$  (measured with thermocouples). The whole assembly is then lowered into the long paths in the space between the interferometer blades. Figure 11 shows a photograph of the coil assembly.

#### G. Polarization analyzer

The polarization state *not* selected by the interferometer goes downstream to the magnetically saturated  $\text{Co}_{0.92}\text{Fe}_{0.08}$  polarization analyzer crystal, where it is reflected by the (111) reflection. The  $\text{Co}_{0.92}\text{Fe}_{0.08}$  crystal is magnetically saturated and held between a pair of  $\text{Nd}_2\text{Fe}_{14}\text{B}$  magnets and mounted in a soft iron yoke to contain the return field. The applied field of the analyzer crystal is the vertical,  $+\mathbf{z}$ , direction, which lies perpendicular to the scattering plane, and represents another orthogonal change in field direction. The analyzer only reflects the  $+\mathbf{z}$  spin component of the neutron beam. We also note that while the interfering beams are polarized, in the geometry of Fig. 5, the analyzed beam is a mixture of both polarization states as the interferometer also transmits a fraction of its accepted state.

### III. EXPERIMENT PREPARATION

#### A. Optimizing alignment

The double-bounce reflector and interferometer must first be aligned to within the Darwin width, and then maintain the stability of this alignment against instabilities due to thermal

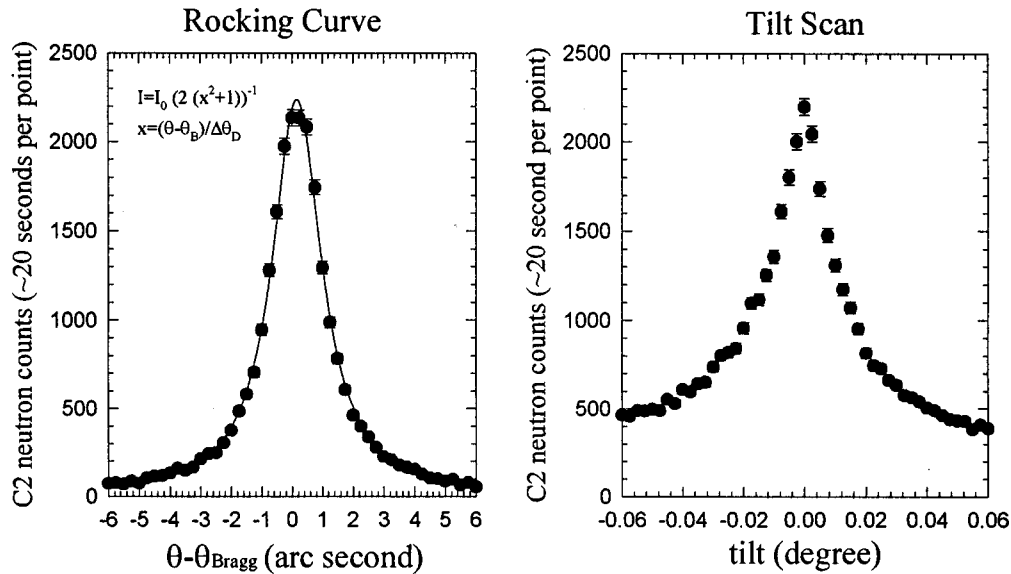


FIG. 12. Plots of a rocking curve and tilt scan for the double-bounce–interferometer assembly. The rocking curve is a convolution of the double-bounce Bragg reflections and the interferometer Laue reflections and transmissions (the FWHM is approximately 2 arc sec). The solid line is a fit based on the Laue profile on which the Bragg profile has little effect.

fluctuations and vibrations to arc sec tolerances. Aligning two 1.6-arc sec reflection volumes in two angular dimensions (rotation and tilt) is no easy task. The initial step aligned the interferometer with the beam direction using two, broad mosaic (width  $0.5^\circ$ ) Si(220) crystals oriented to simulate a perfect double-bounce crystal. Once the interferometer was aligned to the incident beam it was locked in position, and not moved again. A perfect double-bounce crystal was inserted, replacing the mosaic pair. The ensuing procedure was followed any time the two perfect crystals needed realigning. The double-bounce crystal was first driven a good degree off level in tilt. In  $k$  space, this put the two 1.6-arc sec-wide volumes selected by the two crystals at sufficient angle to each other, to find where they overlapped. The alignment then proceeded iteratively using the double-bounce reflector fine rotation stage (a minimum step size of 0.05 arc sec) and the tilt stage to achieve the optimum alignment. In general, realignment of the instrument took less than half an hour, and was performed every 12 h. A rocking curve and a tilt scan, using unpolarized neutrons, at the optimum alignment are shown in Fig. 12. The full width at half maximum (FWHM) is about 2 arc sec, confirming the results of dynamical diffraction calculations. As can be seen in Fig. 12, the integrated intensity falls away quickly, hence the need for such strict tolerances in alignment and stability. Figure 13 shows an interference plot as a function of nuclear phase rotator angle at the optimum alignment. These interferograms confirm that the mean relative intensities of the C2 and C3 detector beams are modified by the pair of Bragg reflections in the double-bounce crystal to something around 2 (the interferometer alone value is 23/9 [32]).

The same alignment procedure is followed for polarized neutrons as, by design, the birefringence of the two polarization states simply splits the double-bounce reflection volume, and only the desired state is aligned to the interferometer. A full description of the alignment process is reciprocal,  $k$  space was given by Lee *et al.* [33]. A rocking curve showing the birefringent splitting of the neutron beam into the two

polarized beams is shown in Fig. 14. A double Gaussian curve fit gives a 3.3-arc sec separation in agreement with calculation [Eq. (22)]. In the experiment, we align the two crystals to the center of one of the two peaks. That is, one of the two polarized beam states satisfies the Bragg reflection condition of the interferometer, while the other polarization state passes through the interferometer without being reflected around the interfering paths. At the center of each peak the tail of the other peak amounts to about 2% of the intensity. In other words, the polarized neutron beam reflected through the interferometer consists of an incoherent mixture of less than 2% (as measured by the polarization

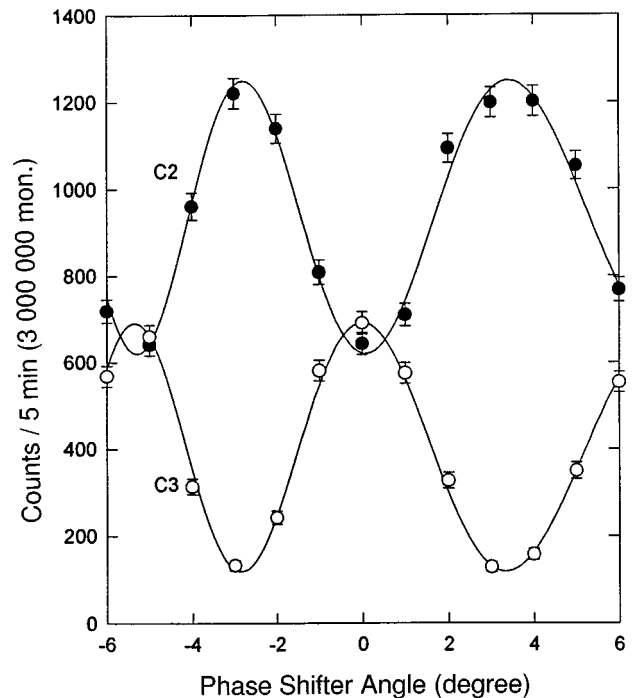


FIG. 13. A nuclear (spin-independent) interferogram as a function of rotation of the optically flat aluminum plate.

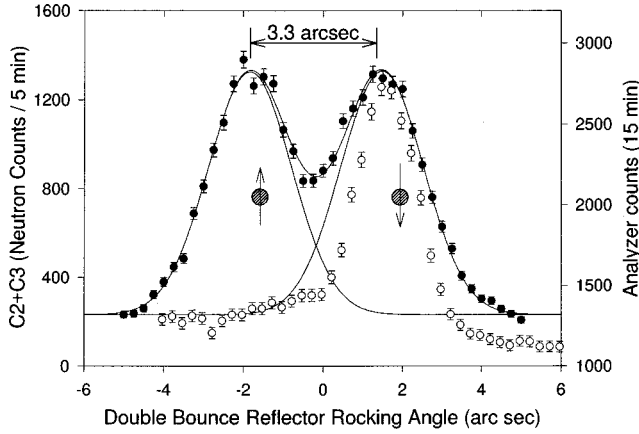


FIG. 14. Rocking curve of the double-bounce reflector against the interferometer, showing the birefringent splitting of the two neutron polarization states by 3.3 arc sec. The lines are Gaussian fits to the data. Overlying the figure are the  $\text{Fe}_{0.08}\text{Co}_{0.92}$  analyzer crystal counts such that only the down-polarized neutrons are accepted.

analyzer behind the interferometer) of the polarized beam of opposite polarization.

### B. Interferometry and polarization

The interferometer measures the relative phase between the two de Broglie subpackets on the separate interferometer paths. The intensity measured in the C2 and C3 detectors are given by

$$I_{C2} = a + Cb \cos[\alpha_0 + \alpha + \sigma(\beta + \beta_{AB})] \quad (24)$$

and

$$I_{C3} = b - Cb \cos[\alpha_0 + \alpha + \sigma(\beta + \beta_{AB})]. \quad (25)$$

In these equations, the intensity parameters are related approximately by  $a \approx 2b$ ; and  $\alpha_0$  is the interferometer offset phase,  $\sigma = \pm 1$  for spins parallel and antiparallel to the applied magnetic field, and  $\beta_{AB}$  is the Aharonov-Bohm phase of interest. To achieve a spin-independent phase shift  $\alpha$  via the nuclear interaction, a 1-mm-thick aluminum plate (nuclear phase rotator) is rotated in beam path II. A magnetic field (static or pulsed) in the “pulse” coil and the guide field shifts the phase of the spin parallel and antiparallel components by equal but opposite amounts  $\beta$ . The fringe visibility is given by the contrast, namely,

$$C = \frac{I_{C3}(\max) - I_{C3}(\min)}{I_{C3}(\max) + I_{C3}(\min) - 2I(\text{background})}, \quad (26)$$

and is at least 0.75 for this experiment.

At issue in the polarized neutron scalar AB is the quantum description of an unpolarized ensemble. Interferometry offers a unique opportunity to elaborate some of these issues. A well-defined pure ensemble of polarized neutrons at an angle  $\theta$  to an applied magnetic field gives an intensity in the C3 detector of

$$\begin{aligned} I_{C3} &= I_{C3\uparrow} + I_{C3\downarrow} = \cos^2 \frac{\theta}{2} [b - Cb \cos(\alpha + \beta)] \\ &+ \sin^2 \frac{\theta}{2} [b - Cb \cos(\alpha - \beta)] \\ &= b - Cb(\cos \alpha \cos \beta - \cos \theta \sin \alpha \sin \beta). \end{aligned} \quad (27)$$

The fractions  $\cos^2(\theta/2)$  and  $\sin^2(\theta/2)$  are the analyzed spin-up and spin-down components of the magnetic field, respectively. If we set the nuclear phase  $\alpha = 0(\text{mod } 2\pi)$ , the magnetic interference pattern generated by changing  $\beta$  becomes independent of polarization, regardless of the value of  $\theta$ , that is,

$$I_{C3} = b - Cb \cos \beta. \quad (28)$$

Pfeiffer [20] called this nondispersive with respect to the spin degree of freedom. It is the fingerprint of the spin- $\frac{1}{2}$  particle. For particles with other spin numbers, there is no arrangement that gives rise to such a phenomenon.

By comparison, we treat unpolarized neutrons as a 50-50 incoherent mixture of spin-up and -down neutrons along any arbitrary direction, which we define by the magnetic field. In computing the intensity, the spin-up and -down neutrons must be considered separately. The intensity is given by

$$\begin{aligned} I_{C3} &= I_{C3\uparrow} + I_{C3\downarrow} = \frac{1}{2} \{b - Cb \cos[\alpha + \beta]\} \\ &+ \frac{1}{2} \{b - Cb \cos[\alpha - \beta]\} \\ &= b - Cb \cos \alpha \cos \beta. \end{aligned} \quad (29)$$

This is the same representation as Eq. (28), for  $\alpha = 0$ . If we have a partially polarized neutron beam of polarization fraction  $f$  then the C3 detector intensity is given by

$$\begin{aligned} I_{C3} &= I_{C3\uparrow} + I_{C3\downarrow} = f[b - Cb \cos(\alpha + \beta)] \\ &+ (1 - f)[b - Cb \cos(\alpha - \beta)]. \end{aligned} \quad (30)$$

If  $f = \cos^2(\theta/2)$ , then we have a result identical to Eq. (27). That is, the interference patterns generated by a pure ensemble at an angle  $\theta$  to the magnetic field and a partially polarized beam with polarization fraction  $f = \cos^2(\theta/2)$  are identical. For the case of a partially polarized beam where both fractions are polarized along a direction at an angle  $\theta$  to the  $\mathbf{B}$  field, we obtain

$$I_{C3} = b - Cb[\cos \alpha \cos \beta + (2f - 1)\cos \theta \sin \alpha \sin \beta]. \quad (31)$$

There are infinitely many combinations of  $(2f - 1)\cos \theta$  that achieve the same interference pattern. Moreover, the intensity (phase shift) can be made independent of the polarization as it was for the perfectly polarized beam by setting  $\alpha = 0$ . Further confirming this phenomenon is a fingerprint of spin- $\frac{1}{2}$  particles.

However, by turning the  $\mathbf{B}$  field to a different direction, the neutron beams prepared by the two different approaches will no longer give identical results: for instance, changing from  $\theta$  to  $\theta + \theta'$  gives

$$I_{C3} = \cos^2 \frac{\theta + \theta'}{2} [b - Cb \cos(\alpha + \beta)] + \sin^2 \frac{\theta + \theta'}{2} [b - Cb \cos(\alpha - \beta)] \quad (32)$$

for the pure ensemble, and

$$I_{C3} = \left( f \cos^2 \frac{\theta'}{2} + (1-f) \sin^2 \frac{\theta'}{2} \right) [b - Cb \cos(\alpha + \beta)] + \left( (1-f) \cos^2 \frac{\theta'}{2} + f \sin^2 \frac{\theta'}{2} \right) [b - Cb \cos(\alpha - \beta)] \quad (33)$$

for partially polarized neutrons. For example, a neutron beam polarized perpendicular to the  $\mathbf{B}$  field may give the same interference pattern as an unpolarized neutron beam. However, turning the  $\mathbf{B}$  field to a different direction changes the interference pattern of the polarized beam, while leaving that for the unpolarized beam unchanged.

If we set  $\beta = \pi/2$ , then a nuclear interferogram of maximum amplitude-to-mean ratio is achieved for  $\theta = 0$  (longitudinal neutrons) which in turn gives the fraction  $f$ . Such a comparison of the amplitude-to-mean ratio for  $\beta = 0$  and  $\beta = \pi/2$  interferograms gave a polarization factor of  $f = 97\%$ , indicating that the experimental optimization of the permanent magnetic fields through the apparatus has successfully maintained the polarization from the 98% at the prism assembly. However, for small  $\theta$ ,  $\cos \theta \approx 1$  and  $f$  cannot be accurately determined. A better technique to determine  $f$  is to use classical polarization analysis in a plane perpendicular to longitudinal where the intensity goes as  $\sin \theta$ , as will now be explained.

### C. Optimizing polarization

Having achieved vertically polarized neutrons (i.e., along  $\hat{z}$ ) in the prism assembly, we now present the verification that the classical polarization of the neutron beam in the interferometer is in fact longitudinal. Consider an arbitrarily polarized neutron beam  $|\chi_{SF}\rangle$  that emerges from the spin flipper. When the neutron subpacket traverses a static longitudinal magnetic field inside the interferometer, the sum of the longitudinal guide field and a static longitudinal  $\mathbf{B}$  field (applied with a dc current) in the ‘‘pulse’’ coil, the neutron spin state (Larmor) precesses by an angle  $\beta/2$ , and the wave function becomes

$$|\chi_P\rangle = \exp(-i\sigma_x \beta/2) |\chi_{SF}\rangle. \quad (34)$$

At the analyzer crystal, the reflected  $+z$  polarization intensity is proportional to

$$|\langle \sigma_{+z} | \chi_P \rangle|^2 \approx I_0 + I_M \sin \theta \cos \beta. \quad (35)$$

In this classical polarization measurement of the analyzer, the counts vary sinusoidally as a function of the static  $\mathbf{B}$  field of the pulse coil, i.e.  $\beta$ , while the amplitude of the sinusoid is proportional to  $\sin \theta$ , where  $\theta$  is the polarization angle (relative to the longitudinal direction). We note that the orientation of the longitudinally polarized neutron when it is ana-

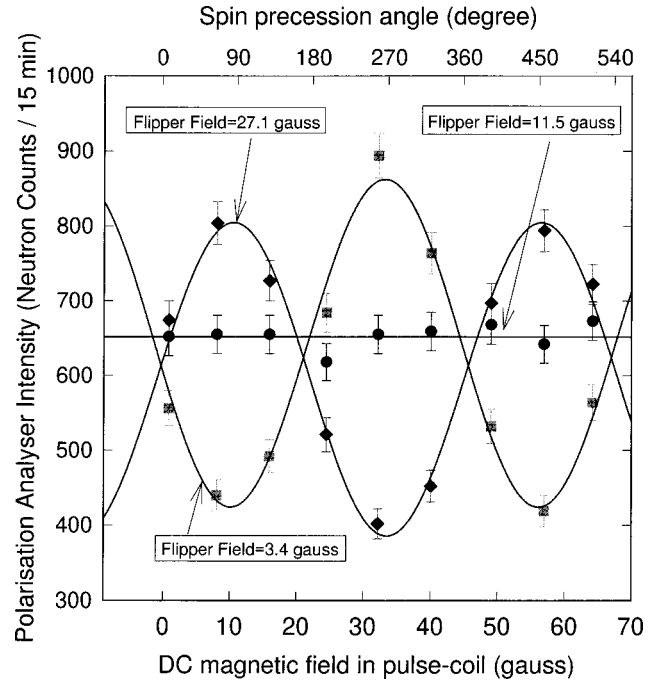


FIG. 15. Determining the classical neutron polarization: The amplitude of the sinusoidal plot is proportional to the angle the classical polarization makes with an applied dc longitudinal magnetic field in the ‘‘pulse’’ coil. The neutrons are polarized precisely longitudinally when the amplitude vanishes (filled circles).

lyzed does not matter; the issue is that it would vary sinusoidally if it was not longitudinally polarized inside the pulse coil. Ideally, however, the neutron is still longitudinally polarized at the analyzer, so  $I_0$  is 50% of the total flux. For the partially (fraction  $f$ ) polarized neutron beam being analyzed,

$$|\langle \sigma_{+z} | \chi_P \rangle|^2 \approx I_0 + f I_M \sin \theta \cos \beta + (1-f) I_M \sin(-\theta) \cos \beta = I_0 + (2f-1) I_M \sin \theta \cos \beta. \quad (36)$$

Only in the case where the neutron has been successfully rotated to a longitudinal polarization ( $\theta = 0$ ) by the spin flipper will the analyzed intensity be independent of  $\beta$ , i.e., independent of the static field  $\mathbf{B}$ . No classical spin precession occurs when longitudinally polarized neutrons pass through the longitudinally oriented static  $\mathbf{B}$  field.

By confirming the independence of the analyzed intensity to  $\beta$ , the operating point of the spin-flipper magnetic-field strength and tilt angle is established. Analyzed intensities for three flipper field strength settings are displayed in Fig. 15, with the 11.5-G field exhibiting the uniform intensity indicative of longitudinally polarized neutrons.

A central issue of this experiment was to have neutrons polarized longitudinally, in the same direction as the pulsed magnetic field. Therefore, a great deal of effort went into establishing a polarized beam and ensuring that we knew its orientation throughout the entire setup. To this end, an experimental optimization of the competing magnetic fields in the transition region from the vertical prism assembly field, via the transverse spin-flipper field to the longitudinal interferometer field, was achieved using the polarized neutrons as a probe of the fields along the beam path. In this manner any differences from the desired configuration were limited to second order.

The polarization fraction was further confirmed by spin-independent interferograms made with longitudinally polarized neutrons. In this case, the intensities in the C2 and C3 detectors is given by

$$I_{C2} = a + Cb[\cos \beta \cos \alpha - (2f - 1)\cos \theta \sin \beta \sin \alpha] \quad (37a)$$

and

$$I_{C3} = b - Cb[\cos \beta \cos \alpha - (2f - 1)\cos \theta \sin \beta \sin \alpha], \quad (37b)$$

respectively.

#### IV. SAB WITH LONGITUDINALLY POLARIZED NEUTRONS

The analysis of the interferograms is simplified by assuming that there is a pure ensemble of neutrons polarized longitudinally along  $+x$  (the contribution to the interference pattern due to the small percentage of  $|\sigma_{-x}\rangle$  neutrons is insignificant). Thereby, the C2 and C3 detector intensities are given by

$$I_{C2} = a + Cb \cos[\beta_{AB} - \alpha - \beta_0] \quad (38a)$$

and

$$I_{C3} = b - Cb \cos[\beta_{AB} - \alpha - \beta_0], \quad (38b)$$

respectively. If there is no magnetic-field bias between the two interferometer arms,  $\beta_0 = 0$ , and the nuclear phase is set at  $\alpha = \pi/2$ , the intensities become

$$I_{C2} = a + CB \sin \beta_{AB} \quad (39a)$$

and

$$I_{C3} = b - Cb \sin \beta_{AB}. \quad (39b)$$

As in the previous scalar AB effect experiment [34], a time-dependent pulsed magnetic field  $\mathbf{B}(t) = \mathbf{B}_{\text{pulse}}(t)\hat{\mathbf{x}}$  is produced by applying a square current sequence to the coil. The current pulse duty cycle is 128  $\mu\text{sec}$ , with two 8- $\mu\text{sec}$  pulses of opposite polarity separated by 64  $\mu\text{sec}$  every cycle. The time-of-flight data as detected by Oxford multichannel scalars with 2- $\mu\text{sec}$  channels for various pulse field strengths are shown in Fig. 16. Each data run was performed at a different magnetic-field setting and lasted 12 h. Afterward the double-bounce and interferometer crystals were realigned and a nuclear interferogram performed to reoptimize the spin-independent phase ( $\alpha = \pi/2$ ). The phase shift acquired by any neutron along the beam path,  $\Delta\beta_{AB}(\mathbf{x}, \mathbf{v})$ , is a convolution of the temporal current pulse and the ‘‘pulse’’ coil spatial field profile. The spatial dependence of the field profile can be converted to a time-of-flight scale by division by the mean neutron velocity  $v$ . In order to faithfully analyze the time-of-flight data, the distribution of neutron wavelengths (and hence speeds), and the detection probability of the 20-atm  $^3\text{He}$  proportional detectors, must also be convolved into the temporal model. The solid line is a one-parameter fit to the whole data set of the plots in Fig. 16.

The SAB phase shift experienced by those neutrons contained in the spatially uniform field at the center of the ‘‘pulse’’ coil for the duration of the pulse is nondispersive

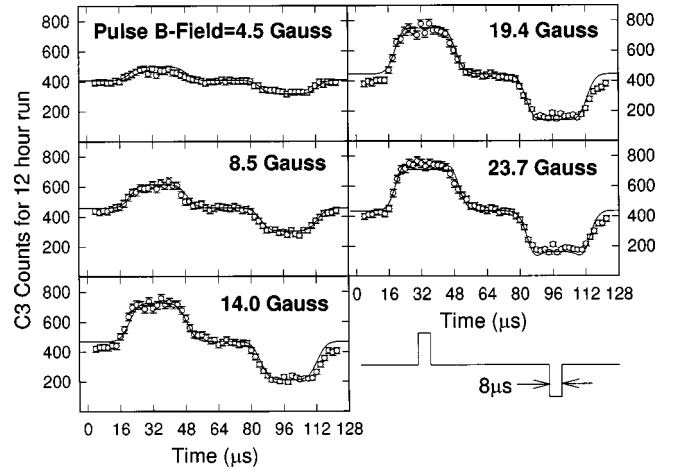


FIG. 16. Scans of the gated neutrons counts in the C3 detector representing the TOF data for both up and down pulses for the range of applied magnetic fields. The plateau at the center of the peaks corresponds to the SAB phase shift. The solid curves are a one parameter fit to the entire data set.

[17]. However, those neutrons at the entrance and exit of the coil when the field is turned on or off experience a dispersive field gradient. The intensity difference between the center six points, well inside the nondispersive region, of the up and down pulses gives

$$I_{C3\text{up}} - I_{C3\text{down}} = 2Cb \sin \beta_{AB}. \quad (40)$$

A plot of these differences showing the expected sinusoidal intensity of the scalar Aharonov-Bohm phase shift is given in Fig. 17, in clear agreement with prediction. The solid line is a fit to the data and corresponds to a pulse width of 7.36  $\mu\text{sec}$ , 3% less than the measured 7.6  $\mu\text{sec}$ .

#### V. SAB WITH UNPOLARIZED NEUTRONS

One of the intents of the current experiment was to perform the unpolarized neutron scalar Aharonov-Bohm experiment [16] again, but using the present exact same geometry to show the measured phase shift is the same as that for the polarized neutron beam. That is, to show that the unpolarized beam is an incoherent mixture of spin-up and spin-down neutrons relative to the applied magnetic field. To perform the unpolarized version, the magnetic prism assembly was removed, and with it the birefringent divergence of the two spin states. The spin flipper remained in place, but was turned off. The quantization axis is established by the direction of the field in the ‘‘pulse’’ coil. However, in the polarized and the original scalar AB experiments uniform environment fields were employed. Therefore, to maintain the geometry, the guide field remained. A second solenoid, the dc ‘‘bias’’ coil, was added to the other beam path (II) to allow separate control over the two spin states, as is now explained. The count rate in the C3 detector for spin-up neutrons is

$$I_{C3\uparrow} = \frac{1}{2}\{b - Cb \cos[\alpha_0 - \alpha + (\beta_{AB} - \beta_0)]\}, \quad (41a)$$

while for spin-down neutrons it is

$$I_{C3\downarrow} = \frac{1}{2}\{b - Cb \cos[\alpha_0 - \alpha - (\beta_{AB} - \beta_0)]\}, \quad (41b)$$

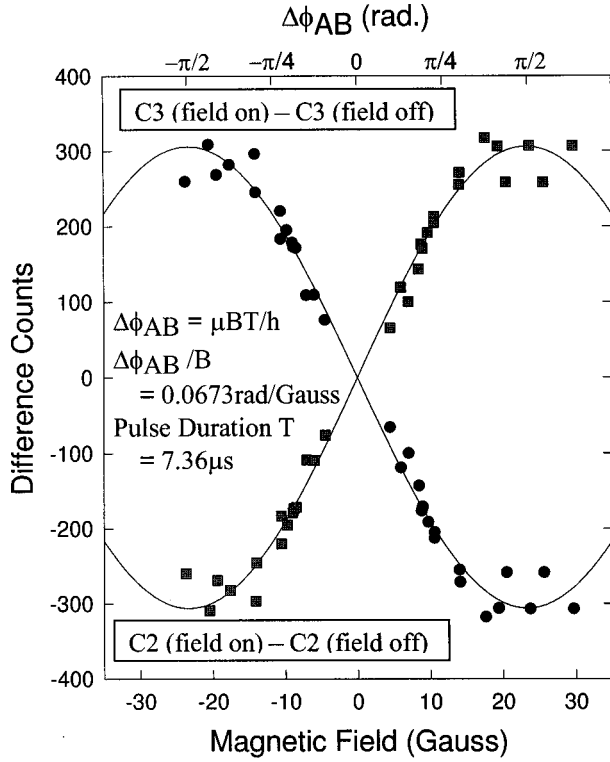


FIG. 17. SAB interference intensity for longitudinally polarized neutrons, shown as the difference in counts between the positive and negative field pulses (certain kinds of systematic error are avoided by taking the difference), as a function of the pulsed field strength. Each point is the average of the central six points in the plateau regions of the data sets shown in Fig. 16, and the error bars are the size of the data points. The solid lines are sinusoidal fits, used to determine the pulse duration.

where  $\alpha_0$  is the offset phase of the interferometer. Therefore, the unpolarized neutron intensity is

$$I_{C3} = b - Cb \cos(\alpha_0 - \alpha) \cos(\beta_{AB} - \beta_0) \quad (42a)$$

in the C3 detector, and, analogously,

$$I_{C2} = a + Cb \cos(\alpha_0 - \alpha) \cos(\beta_{AB} - \beta_0) \quad (42b)$$

in the C2 detector. We have completely decoupled the spin-independent phase from the spin-dependent phase. This is a fact that has been utilized for a good while [11], and ratified again by recent experiment [35]. Setting  $\alpha_0 - \alpha = 0 \pmod{2\pi}$  using the aluminum phase plate and adjusting the dc current to the “bias” coil, so that  $\beta_0 = (n + \frac{1}{2})\pi$ , we have

$$I_{C3} = b - (-1)^n Cb \sin \beta_{AB} \quad (43a)$$

and

$$I_{C2} = a + (-1)^n Cb \sin \beta_{AB}. \quad (43b)$$

A series of time-of-flight (TOF) scans was performed for different pulsed magnetic-field strengths as in the polarized experiment. Again plotting the difference counts from the up and down pulse regions, the sinusoidal dependence of the scalar AB phase shift becomes apparent, as shown in Fig. 18, in complete analogy with Fig. 17. Curve fitting these data

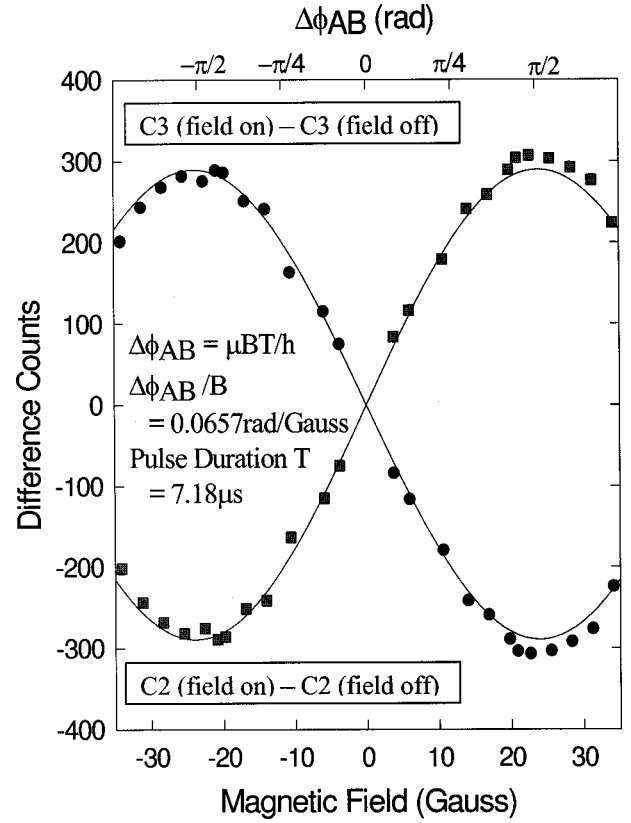


FIG. 18. SAB interference intensity for unpolarized neutrons, shown as the difference in counts between the positive and negative field pulses, as a function of the pulsed field strength. In analogy with the data of Fig. 17, each point is obtained from the plateau regions of TOF data sets, and the error bars are the size of the data points. The solid lines are sinusoidal fits, used to determine the pulse duration.

gives an equivalent pulse on-time of  $7.18 \mu\text{sec}$ , in excellent agreement with the polarized experiment result. Finally, having the unpolarized results to compare with, we note that the polarized data becomes less stable at high fields. This is a consequence of the spin-independent and -dependent phases (and hence intensity) remaining entangled in the polarized experiment. Therefore, the precise measurement of small phase shifts in a polarized geometry remains experimentally difficult.

## VI. DISCUSSION OF THE QUANTUM NATURE OF THIS EXPERIMENT

The force-free setting of the AB experiments leads to nondispersive phase shifts. The polarimetry experiment [17] showed the nondispersive nature of the current experimental geometry by the nondisappearance of the spin-interference contrast. The topological nature of the effect is not so obvious. The topological nature of the AB effects was discussed in Sec. ID in terms of the topological winding number, meaning that the space-time path integral is path independent. Necessarily, the interaction potential has the same value between neighboring paths, or in other words, the gradient of the potential must be zero [36]. The neutrons must traverse the interior of the solenoid, and they have to do it at a certain time. For the SAB effect, nondispersivity requires

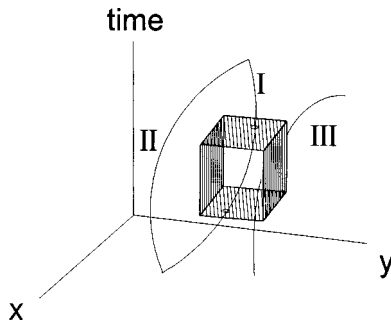


FIG. 19. Space-time representation of the SAB effect. The  $x$ - $y$  plane is the plane containing the neutron paths. The shaded “box” represents the uniform solenoid field in space-time, the vertical dimension being the pulse duration and the horizontal dimensions the spatial extent of the uniform field region. The nondispersivity criterion classifies all paths into three classes: path I represents those neutrons acquiring the nondispersive SAB phase shift, path II does not interact with the potential at all, and path III undergoes a dispersive interaction.

that the scalar potential depend only on time. A space-time trajectory of the interaction is shown in Fig. 19. The  $x$ - $y$  plane is the plane of the neutron flight path, and the vertical axis is time. The shaded “box” represents the uniform solenoid field in space-time, the vertical dimension being the pulse duration and the horizontal dimensions the spatial extent of the uniform field region. Three possible neutron trajectories are shown. The trajectories that give rise to the SAB phase shift are those that traverse the box from bottom to top (labeled I), representing those neutrons inside the solenoid for the duration of the pulse. The paths labeled II do not interact with the potential at all, while the rest (III) transit the potential in its spatial dimensions and undergo a dispersive interaction. For classes I and II, the trajectories within each path are topologically equivalent, but the two classes are not equivalent to each other. All trajectories that undergo a nondispersive interaction are topologically equivalent. Conversely, by virtue of the above dissection, all the topologically equivalent trajectories that interact with the potential undergo a nondispersive interaction. Under such a definition, the topological nature is logically equivalent to nondispersivity, both requiring a time-dependent interaction potential.

A path-dependent energy difference between two space-time points indicates that the interaction is dissipative. This not only provides a classical means by which to observe the effect of the potential, but will also allow the determination of the trajectory of a particle, thus destroying the interference and hence the phase information. Furry and Ramsey [37] found that if the measurement is accurate enough to reveal

the path the particle takes, the uncertainty introduced in the phase shift is sufficient to destroy the interference. All AB effects are therefore nondissipative. For the SAB effect, the particle potential interaction should not induce changes in the pulse-generating circuits that reveal the presence of the particle in the region of interaction to destroy the interference. By using longitudinally polarized neutrons, in this experiment, we have additionally ensured there is no local exchange of angular momentum with the field.

Finally, one further quantum-mechanical aspect of the current experiment, as pointed out recently by Comay [38], is the fact that the neutron’s spin and its associated magnetic moment are properties of a quantum-mechanical system whose state may only vary in quantum leaps. As the excited baryonic states of the neutron are at such high energies, the neutron remains in the ground state during the entire interaction. If however, we performed an analogous classical experiment, replacing the neutron with a current loop, which is free to change state continuously, the Lagrangian becomes independent of the magnetic field  $B$ , and the phase shift disappears.

## VII. CONCLUSIONS

In this paper we have reviewed in detail our neutron interferometric observations, one polarized and one unpolarized, of the scalar Aharonov-Bohm phase shift. We found the two measurements agree with a high precision, as expected, in accordance with the quantum description of an unpolarized beam ensemble. A time-dependent, but spatially uniform, magnetic field was applied to the neutron wave packet in one arm of the interferometer and the phase shift measured by time-of-flight techniques. A process using the birefringence of the neutron polarization in a prism-shaped permanent magnetic field and the arc sec resolution of the Darwin width of a pair of perfect crystals produced the polarized beam. The longitudinally polarized neutrons were determined to be an incoherent mixture of 97%  $|+x\rangle$  and 3%  $|-x\rangle$ , by polarization analysis. There is neither a classical force nor a classical torque acting on the neutrons, so the interference can be explained only by the quantum-mechanical SAB effect, having no classical manifestation or interpretation.

## ACKNOWLEDGMENTS

This work was supported by the NSF Physics Division under Grant No. 9603559. B.E.A. acknowledges support from an Australian Research Council grant during the writing of this paper.

- [1] Y. Aharonov and D. Bohm, *Phys. Rev.* **115**, 485 (1959).
- [2] See for example, M. Peshkin and A. Tonomura, *The Aharonov-Bohm Effect*, Lecture Notes in Physics Vol. 340 (Springer-Verlag, Berlin, 1989); S. Olariu and I. I. Popescu, *Rev. Mod. Phys.* **57**, 339 (1985).
- [3] A. Tonomura, N. Osakabe, T. Matsuda, T. Kawasaki, J. Endo, S. Yano, and H. Yamada, *Phys. Rev. Lett.* **56**, 792 (1986).

- [4] G. Mateucci and G. Pozzi, *Phys. Rev. Lett.* **54**, 2469 (1985).
- [5] D. M. Greenberger, D. K. Atwood, J. Arthur, C. G. Shull, and M. Schenker, *Phys. Rev. Lett.* **47**, 751 (1981).
- [6] Y. Aharonov and A. Casher, *Phys. Rev. Lett.* **53**, 319 (1984).
- [7] P. Hráskó, *Lett. Nuovo Cimento* **2**, 832 (1971).
- [8] P. S. Farago, *Lett. Nuovo Cimento* **5**, 305 (1972).
- [9] A. S. Goldhaber, *Phys. Rev. Lett.* **62**, 482 (1989).

- [10] C. R. Hagen, Phys. Rev. Lett. **64**, 2347 (1990).
- [11] A. Cimmino, G. I. Opat, A. G. Klein, H. Kaiser, S. A. Werner, M. Arif, and R. Clothier, Phys. Rev. Lett. **63**, 380 (1989).
- [12] J. Anandan, Phys. Rev. Lett. **48**, 1660 (1982).
- [13] H. Kaiser, S. A. Werner, R. Clothier, M. Arif, A. G. Klein, G. I. Opat, and A. Cimmino, in *Atomic Physics 12*, edited by Jens C. Zorn and Robert R. Lewis, AIP Conf. Proc. No. 233 (AIP, New York, 1991), p. 247.
- [14] A. Zeilinger, in *Fundamental Aspects of Quantum Theory*, Vol. 144 of *NATO Advanced Study Institute Series B: Physics*, edited by V. Sorini and A. Frigerio (Plenum, New York, 1985).
- [15] J. Anandan, Phys. Lett. A **138**, 347 (1989); **152**, 504 (1991); and in *Proceedings of the Third International Symposium on the Foundations of Quantum Mechanics, Tokyo, 1989*, edited by S. Kobayashi, H. Ezawa, Y. Murayama, and S. Nomura (Physical Society of Japan, Tokyo, 1990), pp. 98–106.
- [16] B. E. Allman, A. Cimmino, G. I. Opat, A. G. Klein, H. Kaiser, and S. A. Werner, Phys. Rev. Lett. **68**, 2409 (1992).
- [17] G. Badurek, H. Weinfurter, R. Gähler, A. Kollmar, S. Wehinger, and A. Zeilinger, Phys. Rev. Lett. **71**, 307 (1993).
- [18] M. Peshkin, Phys. Rev. Lett. **69**, 2017 (1992); M. Peshkin and H. J. Lipkin, *ibid.* **74**, 2847 (1995).
- [19] J. Q. Liang and X. X. Ding, Phys. Lett. A **176**, 165 (1993).
- [20] P. Pfeiffer, Phys. Rev. Lett. **72**, 305 (1994).
- [21] W.-T. Lee, O. Motrunich, B. E. Allman, and S. A. Werner, Phys. Rev. Lett. **80**, 3165 (1998).
- [22] S. Nic Chormaic, Ch. Miniatura, O. Gorcex, B. Viaris de Lesegno, J. Robert, S. Feron, V. Lorent, J. Reinhardt, J. Baudon, and K. Rubin, Phys. Rev. Lett. **72**, 1 (1994).
- [23] K. Sangster, E. A. Hinds, S. M. Barnett, and E. Riis, Phys. Rev. Lett. **71**, 3641 (1993); K. Sangster, E. A. Hinds, S. M. Barnett, E. Riis, and A. G. Sinclair, Phys. Rev. A **51**, 1776 (1995).
- [24] A. Görlitz, B. Schuh, and A. Weis, Phys. Rev. A **51**, R4305 (1995).
- [25] K. Zeiske, F. Riehle, G. Zinner, and J. Helmcke, Appl. Phys. B **60**, 205 (1995).
- [26] B. E. Allman, A. Cimmino, A. G. Klein, H. Kaiser, and S. A. Werner (unpublished).
- [27] N. F. Ramsey, Phys. Rev. A **48**, 80 (1993).
- [28] B. E. Allman, D. L. Jacobson, W.-T. Lee, K. C. Littrell, and S. A. Werner, Nucl. Instrum. Methods Phys. Res. A **412**, 392 (1998). For a more general description of neutron interferometry, see A. G. Klein and S. A. Werner, in *Methods of Experimental Physics*, edited by D. L. Price and K. Skjold (Academic, New York, 1986), Vol. 23A, Chap. 4; H. Rauch and S. A. Werner, *Neutron Interferometry* (Oxford University Press, Oxford, 1999).
- [29] J. B. Hayter, in *Neutron Diffraction*, edited by H. Dachs (Springer-Verlag, Berlin, 1978), Chap. 2.
- [30] G. E. Bacon, *Neutron Diffraction*, 3rd ed. (Oxford University Press, Oxford, 1975), Sec. 6.6, Chap. 15.
- [31] G. Badurek, H. Rauch, and J. Summhammer, Physica B **151**, 82 (1988).
- [32] K. C. Littrell, B. E. Allman, O. I. Motrunich, and S. A. Werner, Acta Crystallogr. A **54**, 563 (1998).
- [33] W.-T. Lee, O. I. Motrunich, B. E. Allman, and S. A. Werner, J. Phys. Soc. Jpn. Suppl. A **65**, 210 (1996).
- [34] B. E. Allman, A. Cimmino, G. I. Opat, A. G. Klein, H. Kaiser, and S. A. Werner, Phys. Rev. A **48**, 1799 (1993).
- [35] A. G. Wagh, V. C. Rakhecha, P. Fisher, and A. Ioffe, Phys. Rev. Lett. **81**, 1992 (1998).
- [36] R. P. Feynman and A. R. Hibbs, *Quantum Mechanics and Path Integrals* (McGraw-Hill, New York, 1965).
- [37] W. H. Furry and N. F. Ramsey, Phys. Rev. **118**, 623 (1960).
- [38] E. Comay, Phys. Lett. A **250**, 12 (1998).